Coherent Anti-Stokes Raman Scattering Imaging of Axonal Myelin in Live Spinal Tissues

Haifeng Wang,* Yan Fu,* Phyllis Zickmund,† Riyi Shi,*† and Ji-Xin Cheng*
*Weldon School of Biomedical Engineering, and †Department of Basic Medical Sciences, Institute for Applied Neurology and Center for Paralysis Research, Purdue University, West Lafayette, Indiana 47907

ABSTRACT We present a vibrational imaging study of axonal myelin under physiological conditions by laser-scanning coherent anti-Stokes Raman scattering (CARS) microscopy. We use spinal cord white matter strips that are isolated from guinea pigs and kept alive in oxygen bubbled Krebs' solution. Both forward- and epi-detected CARS are used to probe the parallel axons in the spinal tissue with a high vibrational contrast. With the CARS signal from CH_2 vibration, we have measured the ordering degree and the spectral profile of myelin lipids. Via comparison with the ordering degrees of lipids in myelin figures formed of controlled lipid composition, we show that the majority of the myelin membrane is in the liquid ordered phase. By measuring the myelin thickness and axon diameter, the value of *g* ratio is determined to be 0.68 with forward- and 0.63 with epi-detected CARS. Detailed structures of the node of Ranvier and Schmidt-Lanterman incisure are resolved. We have also visualized the ordering of water molecules between adjacent bilayers inside the myelin. Our observations provide new insights into myelin organization, complementary to the knowledge from light and electron microscopy studies of fixed and dehydrated tissues. In addition, we have demonstrated simultaneous CARS imaging of myelin and two-photon excitation fluorescence imaging of intra- and extraaxonal Ca^{2+}. The current work opens up a new approach to the study of spinal cord injury and demyelinating diseases.

INTRODUCTION

The combination of nonlinear optical spectroscopy and scanning microscopy has generated a series of new tools for imaging live cells and tissues with three-dimensional (3D) spatial resolution and large penetration depth (1). Among these tools, two-photon excitation fluorescence (TPEF) microscopy (2) has been widely used for in vivo imaging (3,4). Second harmonic generation microscopy (5) has opened up a new way for probing membrane potential and structural proteins (6,7). For molecules that cannot tolerate fluorophore labeling, coherent anti-Stokes Raman scattering (CARS) microscopy (8–10) permits vibrational imaging of specific molecules in unstained samples. CARS is a four-wave mixing process in which the interaction of a pump field $E_p(\omega_p)$ and a Stokes field $E_s(\omega_s)$ with a sample generates an anti-Stokes field E_{as} at frequency $2\omega_p - \omega_s$ (11). The CARS signal is significantly enhanced when $\omega_p - \omega_s$ is tuned to a Raman band, creating the vibrational contrast. Because of its coherent property, the CARS signal increases quadratically with respect to the number of vibrational oscillators in the focal volume. CARS microscopy has been applied to the study of single bilayers (12), polymer films (13), and lipid droplets in adipocyte cells (14).

In this article, we explore the ability of CARS microscopy to probe axonal myelin in live spinal cord white matter isolated from guinea pigs. Presently, the major tools used for spinal tissue observation are light microscopy and electron microscopy (EM), in which the samples are fixed and stained with toluidine blue or other agents, embedded in paraffin or plastic, dehydrated, and then cut into thin sections. The perturbation to the axon structures by the sample preparation procedure could complicate the data interpretation. One such example is the measurement of the *g* ratio defined as the ratio of the inner to the outer myelin fiber diameter. It has been pointed out that dehydration may shrink the myelin sheath (16). Thus the *g* ratio in the EM might be different from the *g* ratio of axons in their natural state. Moreover, dynamic processes such as demyelination cannot be followed in real time using fixed tissues. For characterization of injured spinal tissues, it is hard to discriminate whether the observed changes are from the injury or induced by the sample preparation. An approach to imaging live spinal tissues would help us to overcome these difficulties.

The axons in the central nervous system are generally myelinated (15). The myelin is formed of wrapped oligodendroglial cell membranes and contains ~70% lipid and 30% protein by weight (16). Raman spectroscopy has been used to measure the spectral profile of myelin lipids without dehydration (17). However, the sensitivity of Raman microscopy is not adequate for high-speed imaging of live spinal tissues. On the other hand, the high density of CH_2 groups in myelin leads to a large and directional CARS signal without any labeling. Using the resonant CARS signal from CH_2 or H_2O stretch vibration, we present a systematic imaging study of neuronal myelin under physiological conditions. The potentials of CARS microscopy for studies of spinal cord injury and demyelinating diseases are discussed.

Submitted February 24, 2005, and accepted for publication April 11, 2005.
Haifeng Wang and Yan Fu contributed equally to this article.
Address reprint requests to Ji-Xin Cheng, E-mail: jcheng@purdue.edu.

0006-3495/05/07/581/11 $2.00
doi: 10.1529/biophysj.105.061911

MATERIALS AND METHODS

Sample preparation

Fresh spinal cord samples were isolated from guinea pigs as shown in Fig. 1 *A* (18,19). The spinal cord was first split into two halves by saggital division and then cut radially to separate the ventral white matter from the gray matter. The isolated ventral white matter strip was mounted on a chambered glass cover slip and kept in oxygen bubbled Krebs' solution (NaCl 124 mM, KCl 2 mM, KH_2PO_4 1.2 mM, $MgSO_4$ 1.3 mM, $CaCl_2$ 2 mM, dextrose 10 mM, $NaHCO_3$ 26 mM, and sodium ascorbate 10 mM, equilibrated with 95% O_2, 5% CO_2). The samples for CARS imaging of axonal myelin were not labeled. The samples for simultaneous CARS imaging of axonal myelin and TPEF imaging of Ca^{2+} were incubated in a Ca^{2+} free Krebs' solution that contained 40 μM Oregon green 488 (BAPTA-2, Molecular Probes, Eugene, OR) for 2 h and then washed with normal Krebs' solution (containing 2 mM Ca^{2+}) before imaging. The axons in the sample maintained good morphology for at least 10 h in the chamber.

Dioleoyl phosphatidylcholine (DOPC) and dipalmitoyl phosphatidylcholine (DPPC), and cholesterol were purchased from Avanti Polar Lipids (Alabaster, AL) and used without further purification.

CARS and TPEF imaging

A schematic of the microscope is shown in Fig. 1 *B*. The pump and Stokes beams are generated from two Ti:sapphire oscillators (Mira 900, Coherent, Santa Clara, CA). Both lasers are tunable from 700 to 1000 nm, where water absorption is minimized. The pulse width is 2.5 ps. The corresponding spectral width matches the line width of the CH_2 symmetric stretch Raman band. The two lasers are tightly synchronized (Sync-Lock, Coherent) with an average timing jitter of 100 fs. A Pockels cell is used to lower the repetition rate, which reduces average power but maintains high peak power at the sample. The laser beams are collinearly combined and directed into a laser scanning confocal microscope (FV300/IX70, Olympus America, Melville, NY). A 60× water immersion objective (N.A. = 1.2) is used to focus the excitation beams into the sample. The forward-detected CARS (F-CARS) signal is collected by an air condenser (N.A. = 0.55). The epi-detected CARS (E-CARS) signal is collected by the same water immersion objective. The same picosecond laser beams are also used for TPEF imaging. The epi-detected TPEF signal is spectrally separated from the E-CARS signal by a dichroic splitter. Both CARS and TPEF signals are detected with the same type of photomultiplier tube (PMT, R3896, Hamamatsu, Japan). For epi-detection, we have removed the pinhole used for confocal imaging because both CARS and TPEF microscopy provide inherent 3D spatial resolution. All the imaging experiments were conducted at room temperature, 22°C.

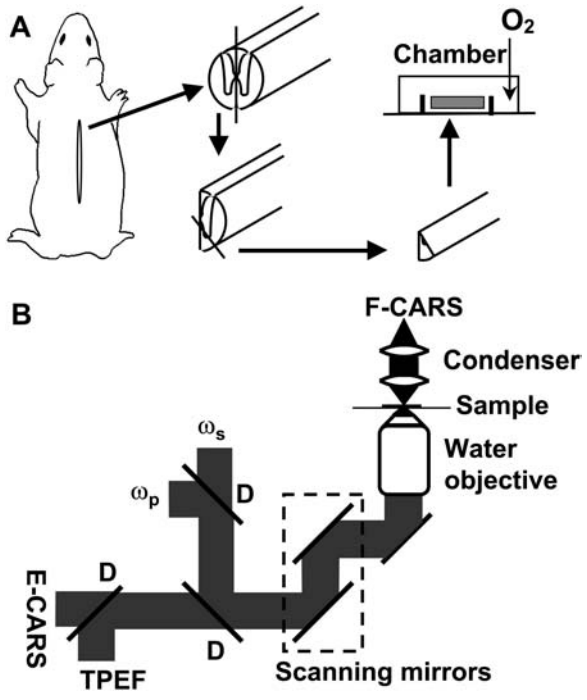

FIGURE 1 (*A*) The sample preparation procedure. (*B*) Schematic of the microscope for simultaneous F-CARS, E-CARS, and TPEF imaging. D, dichroic mirror.

To obtain the CARS spectrum of a single myelin sheath, we acquired a series of CARS images of the same axon at different Raman shifts. We fixed the pump wavelength and manually tuned the Stokes wavelength. The CARS intensity at each Raman shift was normalized by the peak power of the Stokes beam.

The polarization sensitivity of CARS was used to characterize the orientation of the lipid and water molecules inside the myelin sheath. The Raman scattering from liquid water is mainly contributed by the symmetric H_2O stretch vibrational mode (20). The symmetric CH_2 stretch vibration in lipids gives a strong CARS signal (21). For the symmetric CH_2 or H_2O vibration, when the excitation polarization is parallel with or perpendicular to the symmetry axis, the resonant CARS field is contributed by the α_{11} or α_{33} component of the Raman tensor, respectively. Because α_{33} is much smaller than α_{11}, the CARS signal is maximized when the dipole of CH_2 or H_2O is parallel with the excitation polarization, and minimized when the dipole is perpendicular to the excitation polarization. From CARS images of the same sample with *x*- and *y*-polarized excitation fields, one can determine the orientation and ordering degree of lipid and water molecules in the myelin. No polarizers were used before the detectors except for the F-CARS signal polarization measurements.

We also acquired the CARS images of a bare coverslip, which only generates nonresonant CARS. The nonresonant signal is independent of molecular orientation and vibration frequency, but varies with the excitation intensity and detection efficiency at different wavelengths. To rule out the dependence of the CARS intensity on the setup, we normalized the CARS signal from the sample with the nonresonant CARS signal from the coverslip.

RESULTS

F-CARS and E-CARS imaging of myelin

The parallel axonal myelin displays a high contrast in both the F-CARS (Fig. 2 *A*) and E-CARS (Fig. 2 *B*) images. The focal depth is ~100 μm from the bottom of the chamber. The resonant CARS is generated from the stretch vibration of the CH_2 groups inside the myelin sheath. As shown in the intensity profiles below the images, little water background is detected in either F- or E-CARS channels. In most places, the laser beams are focused at the equatorial plane of the axon, where the CARS radiation from myelin sheath predominantly goes forward (Fig. 2 *C*). In this case, the E-CARS signal arises from the back-reflected F-CARS signal by the myelin/fluid interface. The forward CARS signal is partially scattered by the 2-mm-thick spinal tissue. As a result, the average intensity of F-CARS is 18.9 times that of E-CARS when the same high voltage is applied to both detectors. In some places, the laser beams are focused at the top or bottom of the myelin fibers. There the average F- to E-CARS intensity ratio is 2.9, much smaller than the

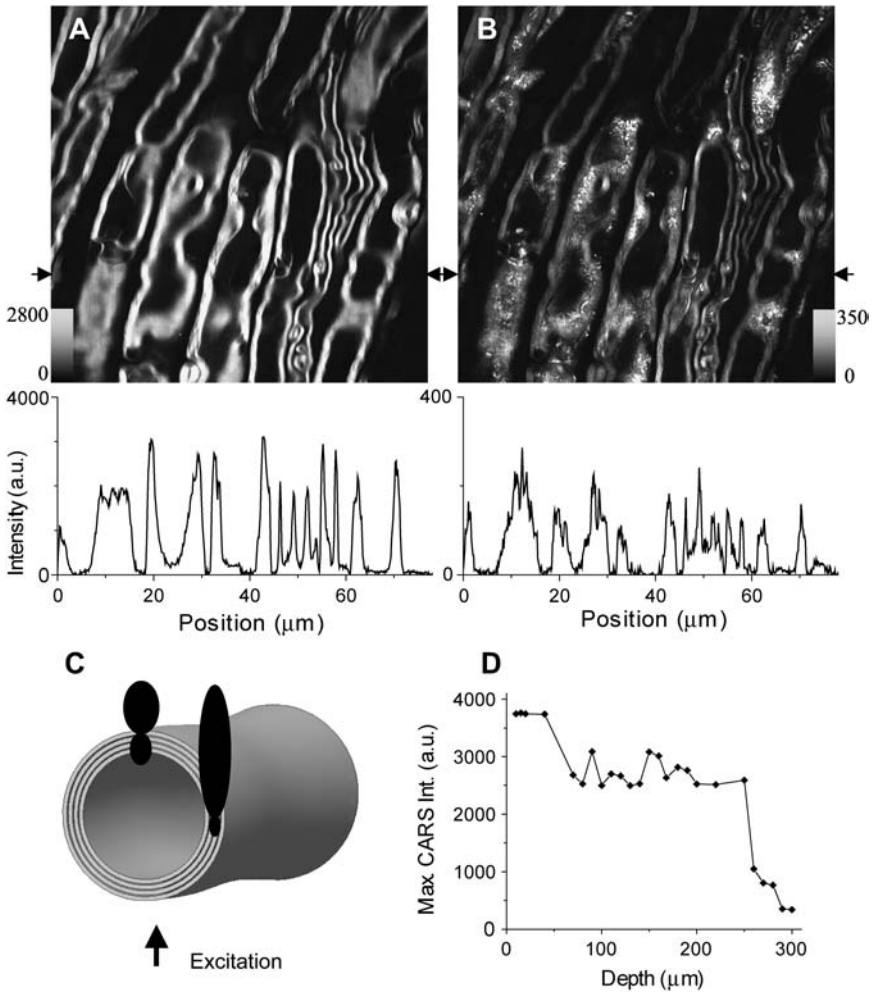

FIGURE 2 (*A*) F-CARS and (*B*) E-CARS images of axons in a spinal cord sample. The pump and Stokes laser frequencies were tuned to 14,318 cm^{-1} (698.4 nm) and 11,478 cm^{-1} (871.2 nm), respectively, producing a wavenumber difference of 2840 cm^{-1}. Each image of 512 × 512 pixels was an average of 10 scans. The total acquisition time was 11.2 s. The PMT high voltage was 510 V for both E-CARS and F-CARS. The pump and the Stokes laser power at the sample were 4.0 and 2.2 mW, respectively, at a repetition rate of 3.85 MHz. Similar powers were used for other CARS images. No photodamage was observed under the applied excitation power and imaging speed. The intensity profiles along the lines indicated by arrows are shown below the images. Note in panel *B*, there are a number of bright dots near the myelin surface. (*C*) Schematic radiation profile of CARS from the top and equatorial part of a myelin fiber. (*D*) The maximal CARS intensity from a single myelin sheath as a function of depth defined as the distance between the focus and the top surface of the bottom coverslip.

ratio for the equatorial area. Additionally, we observed a number of bright dots near the myelin surface (Fig. 2 *B*). These two observations result from the sensitivity of E-CARS to small objects or interfaces perpendicular to the optical axis (22).

Fig. 2 *D* shows the maximal CARS intensity as a function of the focal depth. The maximal depth we have reached to obtain a clear contrast of parallel axons is 250 μm. Due to the limited working distance (280 μm) of our objective lens, the signal rapidly drops when the depth is larger than 250 μm. Although the spatial resolutions of a laser-scanning CARS microscope could be measured by using small beads embedded in agarose gel (23), the values might be different when a tissue sample is dealt with. Therefore, we estimated the resolution of our setup using the same spinal samples under study. The minimal lateral full-width at half-maximum (FWHM) of a single myelin sheath was found to be 0.28 μm in E-CARS images. We approximate this value as the lateral resolution of E-CARS. Because it is difficult to discriminate the upper and lower myelin sheath of a small axon in depth, a large axon was used to determine the axial resolution. The epi-detected lateral and axial FWHMs of a myelin were measured to be 0.56 and 0.85 μm. The myelin thickness is calculated as $\sqrt{0.56^2 - 0.28^2} = 0.49\,\mu$m. The axial resolution is estimated to be $\sqrt{0.85^2 - 0.49^2} = 0.70\,\mu$m. The spatial resolution for F-CARS is found to be similar.

Spectral profile

The E-CARS spectrum of a single axonal myelin is shown in Fig. 3. The peak for the symmetric CH_2 stretch vibration appears at 2840 cm^{-1}, with a resonant signal to nonresonant background ratio of 10:1. Additionally, we observed a weak band at 2930 cm^{-1}, which was also found in the Raman spectrum of myelinated sciatic nerves (17). Because this band is much weaker in the multiplex CARS spectrum of DSPC liposomes (21), we assign it to the CH_3 stretch mode of the proteins that constitute 30% of the weight of the myelin sheath.

Polarization characterization of myelin lamellar structure

The concentric lamellar structure of myelin sheath has been established based on the observations of fixed tissues by

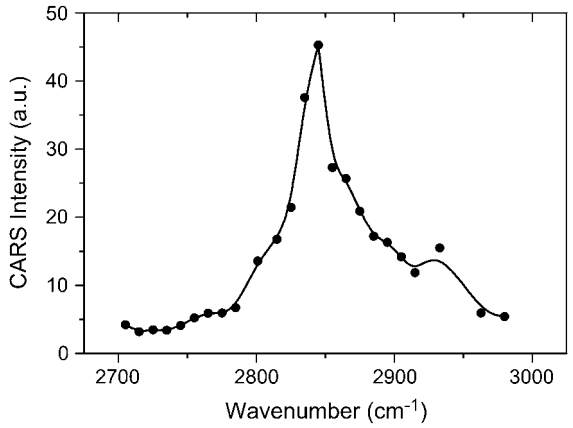

FIGURE 3 E-CARS spectrum of a single axonal myelin sheath measured by manually tuning the Stokes laser wavelength. The pump laser frequency was fixed at 14,081 cm^{-1}.

electron microscopy and x-ray diffraction (16). With the polarization sensitivity of CARS, we are able to examine the orientation of lipid and water molecules inside the myelin sheath under physiological conditions. Fig. 4, *A* and *B*, show the F-CARS images of *y*-oriented axons with $\omega_p - \omega_s$ tuned to 2840 cm^{-1}. The average CARS intensity from the equatorial plane generated with *y*-polarized beams is 3.53 ($\pm$0.09) times that with *x*-polarized beams. We define $I_{\parallel}$ and $I_{\perp}$ as the CARS intensities with the excitation polarization parallel with or perpendicular to the myelin length. $I_{\parallel}$ is larger than $I_{\perp}$ because the symmetry axis of the CH_2 groups in the equatorial plane of the myelin is perpendicular to the *x* direction (Fig. 4 *C*). Because the nonresonant background is much smaller than the resonant CARS signal (Fig. 3), the ratio of $I_{\parallel}$ to $I_{\perp}$ measures the ordering degree of the myelin lipids. The average $I_{\parallel}/I_{\perp}$ for E-CARS is 2.43 ($\pm$0.10), smaller than the F-CARS measurement due to the scrambling of the E-CARS polarization. At the top or bottom of myelin, neither E-CARS nor F-CARS is dependent on the excitation polarization because the CH_2 groups there are oriented along all directions in the *x*-*y* plane.

With $\omega_p - \omega_s$ tuned to the CARS peak for the symmetric H_2O stretch vibration at 3200 cm^{-1} (24), we are able to probe the resonant CARS signal from water molecules inside the myelin sheath. For a *y*-oriented axon (position *2* in Fig. 5), the CARS intensity with *x*-polarized excitation beams ($I_{\perp}$) is stronger than that with *y*-polarized beams ($I_{\parallel}$), opposite to the polarization dependence for the CH_2 signal. This proves

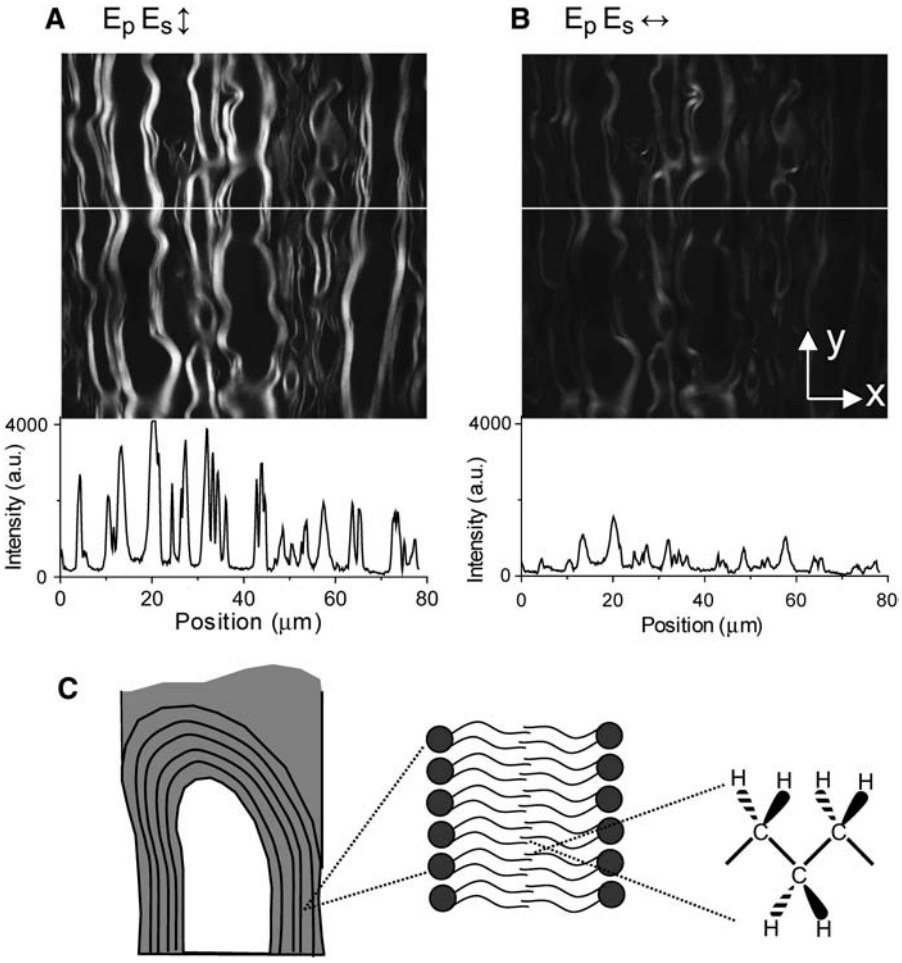

FIGURE 4 F-CARS images of myelin sheath using vertically polarized (*A*) and horizontally polarized (*B*) excitation beams. $\omega_p - \omega_s$ was tuned to 2840 cm^{-1}. The plots below the images are the intensity profiles for the lines shown in the images. (*C*) The symmetry axis of the CH_2 groups in the equatorial plane of the myelin is perpendicular to the *x* direction, leading to a larger $I_{\parallel}$ than $I_{\perp}$.

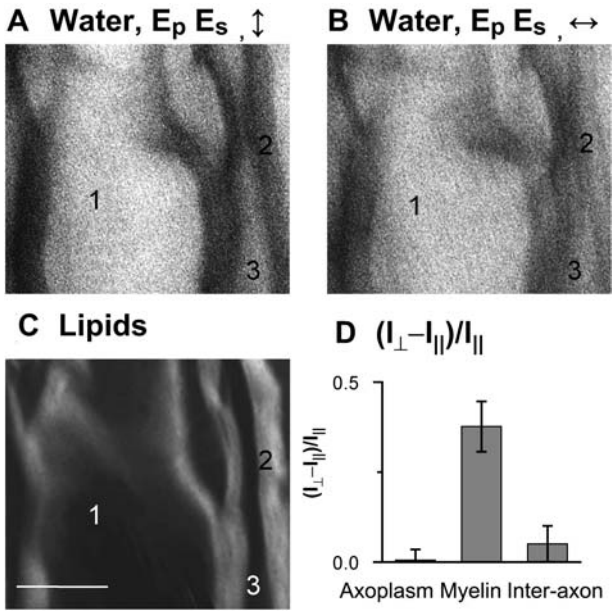

FIGURE 5 (*A* and *B*) F-CARS images of water with the excitation polarization parallel with and perpendicular to the axons, respectively. $\omega_p - \omega_s$ was tuned to 3200 cm^{-1} (*C*) CARS image of the same sample with $\omega_p - \omega_s$ tuned to 2840 cm^{-1}. Bar = 5 μm. Positions *1*, *2*, *3* indicate the location of water in the axoplasm, myelin, and interaxon space, respectively. (*D*) The average values of $(I_\perp - I_\parallel)/I_\parallel$ are 0.005, 0.37, 0.05 for the water molecules in the axoplasm, myelin, and interaxon space, respectively, indicating the ordering of water inside the myelin.

that the intramyelin water molecules are partially ordered with the symmetry axis perpendicular to that of the CH_2 groups.

The ordering of myelin water is further quantified by the following analysis. $I_\perp$ is contributed by the nonresonant CARS ($\mathbf{E}_{NR}$), resonant CARS from isotropic water ($\mathbf{E}_{iso}$), and resonant CARS from ordered water with orientation along the excitation polarization ($\mathbf{E}_{order}$), $I_\perp \propto |\mathbf{E}_0 + \mathbf{E}_{order}|^2$. The ordered water does not contribute to $I_\parallel \propto |\mathbf{E}_0|^2$. Here $\mathbf{E}_0$ is the addition of $\mathbf{E}_{NR}$ and $\mathbf{E}_{iso}$. Because water is a weak Raman scatterer, we have $|\mathbf{E}_0| > |\mathbf{E}_{order}|$. In this case, $(I_\perp - I_\parallel)/I_\parallel$ is approximately proportional to $2|\mathbf{E}_{order}/\mathbf{E}_0|$, which represents the number of ordered water molecules in the excitation volume. As shown in Fig. 5 *D*, the value of $(I_\perp - I_\parallel)/I_\parallel$ is 0.37 for the myelin, indicating the existence of ordered water molecules inside the myelin sheath. For bulk water in the axoplasm area (position *1* in Fig. 5) or the interaxon space (position *3* in Fig. 5), the values of $(I_\perp - I_\parallel)/I_\parallel$ are close to zero. We notice that the N-H stretch vibration is also located in the 3200 cm^{-1} region. To verify the origin of the observed polarization dependence, we incubated the sample with D_2O and measured the CARS intensities from the myelin sheath at 3200 cm^{-1}. The value of $(I_\perp - I_\parallel)/I_\parallel$ is found to be lowered by four times, indicating that the polarization dependence shown in Fig. 5 is primarily not contributed by the N-H vibration in myelin proteins.

Measurements of *g* ratio

It has been realized for a long time that the thickness of the myelin sheath is related to the axon diameter (25). The *g* ratio, defined as the ratio of the inner diameter to the outer diameter, presents the precise relation between the axon diameter and the myelin sheath thickness. The *g* ratio has been widely measured by EM studies of fixed tissues. For example, the mean *g* ratio of optic nerves from a guinea pig was determined to be 0.81 (26).

The CARS signal from myelin provides a way to measure the thickness of myelin sheath in live tissues. An F-CARS image of parallel axons with various diameters and myelin thickness is shown in Fig. 6 *A*. The axons with the diameter <0.53 μm represent a minority $<4\%$ (26). The lateral resolution of our CARS setup is 0.28 μm. Therefore, most axons can be used to calculate the *g* ratio. In our experiment, the myelin thickness is measured as the FWHM of the intensity profile across the equatorial plane of the axonal myelin. This also determines the inner and outer borders of each myelin, which are then used to determine the inner diameter *a* and outer diameter *b* (Fig. 6 *B*).

Fig. 6, *C* and *D*, show that the *g* ratio is 0.68 and 0.63 measured with F-CARS and E-CARS, respectively. These values are in the range between 0.60 and 0.80, the optimal *g* ratio range for attaining effective internodal spread of current with interspecies variation (27). Our measurement is smaller than the value from EM studies ($g = 0.81$). Such difference may arise from the shrinking of myelin sheath during the tissue dehydration process, which reduces the difference between *a* and *b* and increases the *g* ratio consequently. For the same reason, the repeat distance of the myelin lamellar structure measured by EM is smaller than that measured by x-ray diffraction (16).

The *g* ratio measured with F-CARS is 8% bigger than that with E-CARS due to the different signal generation mechanisms between F- and E-CARS. Near the inner and outer myelin surface at the equatorial plane, the focusing of the beams is perturbed by the interface, leading to a sharper decrease of the F-CARS signal. On the other hand, E-CARS is more sensitive to interfaces (cf. Fig. 2). The combination of the two factors leads to a broader intensity profile (Fig. 6 *E*) of myelin sheath in E-CARS than in F-CARS and results in a larger *g* ratio in F-CARS.

Characteristic structures in single myelin

Besides imaging the highly compact myelin sheath, we are also able to probe the less compact structures including the node of Ranvier and the Schmidt-Lanterman incisure. Fig. 7 *A* shows the CARS image of a node of Ranvier by which two adjacent segments of myelin on one single axon are separated. In the paranodal region, we have observed the lateral loops where the cytoplasmic surfaces of myelin are not compact and the myelin forming cell cytoplasm is

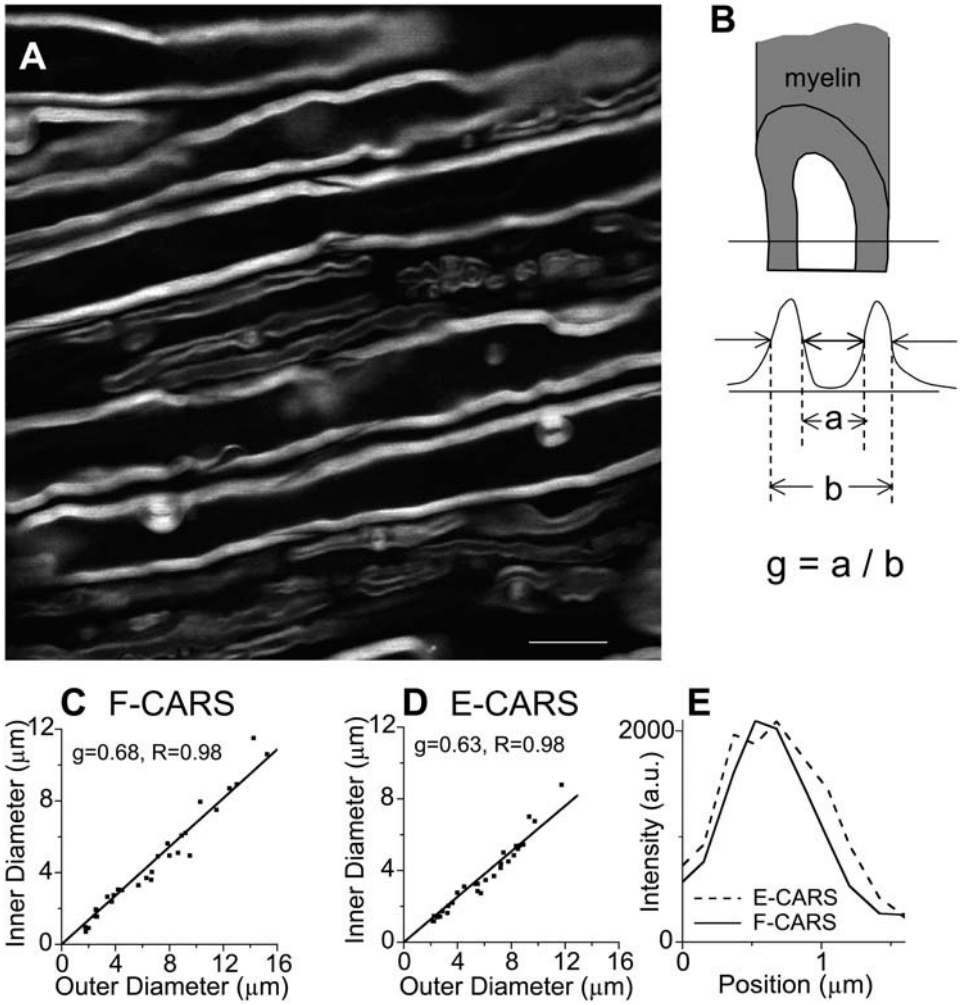

FIGURE 6 (*A*) F-CARS image of axonal myelins with different thickness. $\omega_p - \omega_s$ was tuned to 2840 cm^{-1}. Bar = 10 μm. (*B*) Diagram of measuring the *g* ratio from CARS images. (*C*) The *g* ratio measured with F-CARS images. (*D*) The *g* ratio measured with E-CARS images. (*E*) An example of the E-CARS and F-CARS intensity profiles across a single myelin.

included within the sheath. The axon diameter is ~11 μm in the internodal region and 2 μm in the nodal region, in agreement with EM observations (28). Although CARS microscopy has the sensitivity to probe single membranes (12,23), the signal from a single membrane could be easily buried by the strong contrast from the myelin sheath, making it difficult to obtain CARS contrast for the non-myelinated axon membrane in the nodal region. Fig. 7 *B* shows the F-CARS image of a Schmidt-Lanterman incisure in which layers of myelin are separated by the cytoplasm of oligodendrocyte cells. The lateral loops in the Schmidt-Lanterman incisure are clearly recognized. When the laser beams were focused at the top or bottom of Schmidt-Lanterman incisures, we observed an annular arrangement that winds through the myelin sheath (Fig. 7 *C*). A similar structure has been visualized by using the monosialoganglioside immunofluorescence (29). The capability of probing the node of Ranvier and the Schmidt-Lanterman incisure opens up a new way of investigating biological activities in such areas (30).

Simultaneous imaging of myelin and Ca^{2+}

Fig. 8 demonstrates simultaneous CARS imaging of axonal myelin and TPEF imaging of Oregon green 488, a calcium indicator. The TPEF signal is mainly contributed by the 2.5-ps pump laser beam at 710 nm. In our setup, the lateral and axial resolution for TPEF imaging are 0.45 and 0.85 μm, respectively, measured with 0.2 μm fluorescent beads. As we have mentioned, the lateral and axial resolution of our setup is 0.28 and 0.70 μm, respectively, measured with the intensity profiles of myelin sheath. Therefore, for the myelinated axons with a diameter of a few microns, we are able to visualize the Ca^{2+} distribution inside and outside of individual axons with their boundary defined by the CARS contrast. The intensity profile below the image exhibits a strong TPEF signal in the extracellular space between the parallel axons, while the intraaxonal Ca^{2+} is barely detectable. This indicates a much lower free Ca^{2+} concentration inside the healthy axon than in the extracellular space (31).

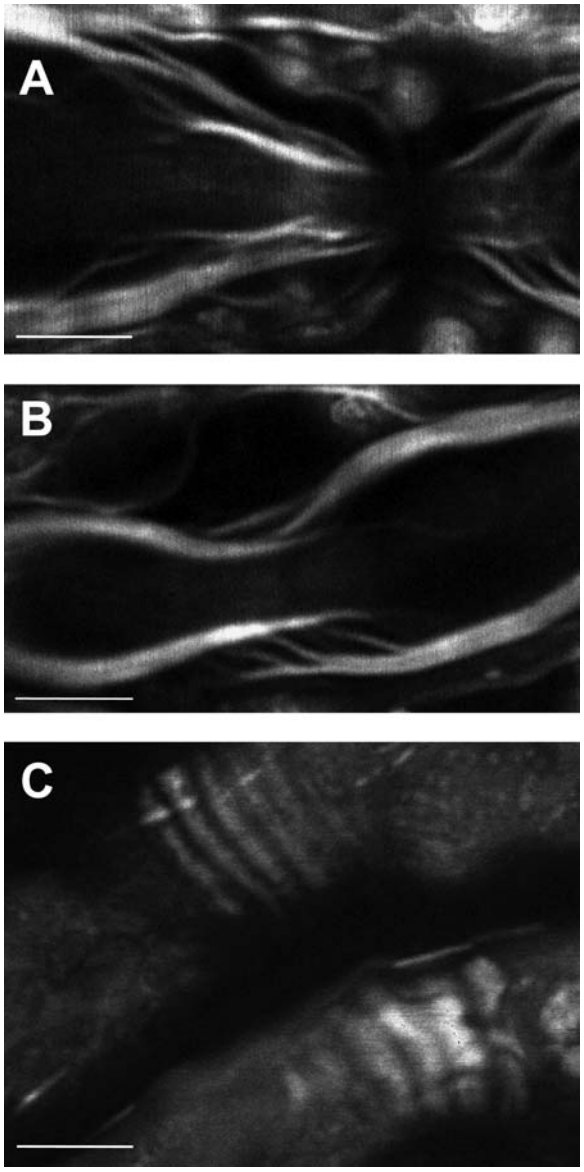

FIGURE 7 Characteristic structures in single live axons visualized by CARS microscopy. $\omega_p - \omega_s$ was tuned to 2840 cm^{-1}. (*A*) F-CARS image of the node of Ranvier; (*B*) F-CARS image of Schmidt-Lanterman incisure; (*C*) E-CARS image of the incisure gap junction locating sites. Bar = 5 μm.

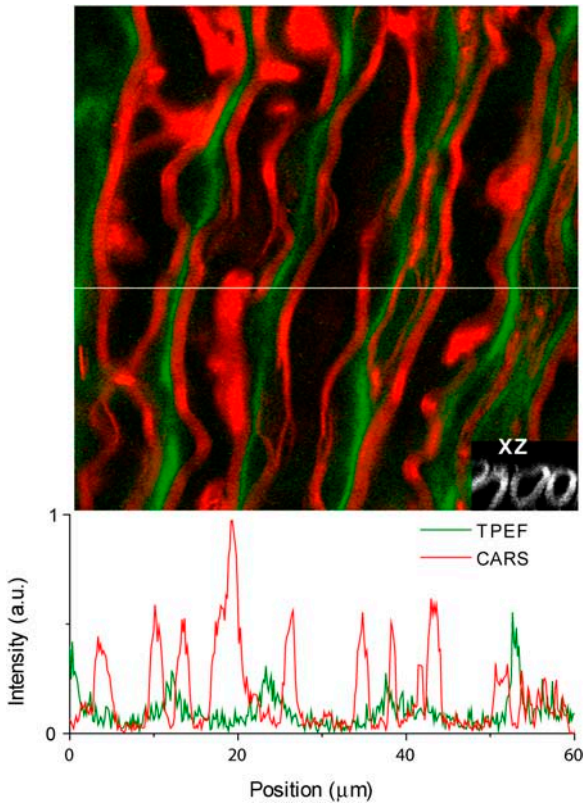

FIGURE 8 Simultaneous CARS imaging of axonal myelin and TPEF imaging of Oregon green 488. The pump and Stokes laser frequencies were tuned to 14,088 cm^{-1} (710 nm) and 11,248 cm^{-1} (889 nm), respectively. The E-CARS and TPEF signals are represented by the red and green colors, respectively. The intensity profiles along the white line are shown below the image. The grayscale inset image is an *XZ* image showing the cross section of axons. The 3D spatial resolution of CARS microscopy permits discrimination of the intraaxonal from extraaxonal space.

DISCUSSION

New insight into molecular organization of myelin

Most of our knowledge about myelin structures comes from studies done with polarized light microscopy, EM, and x-ray diffraction. The sample fixation and dehydration for light and electron microscopy observations may perturb the myelin structure and composition. For example, it was reported that digitonin needs to be used to preserve cholesterol in dehydrated tissues to produce Maltese cross patterns in polarization microscopy (32). CARS imaging of myelin sheath in live spinal tissues avoids any perturbation by the sample fixation procedure and permits more accurate measurements of various parameters such as the *g* ratio. Furthermore, the CARS data provide new insights into the molecular organization of myelin.

Lipid membranes can exist in the liquid disordered (L_d) and the solid ordered (S_o) phases. Incorporation of cholesterol to the bilayer creates a new phase called liquid ordered (L_o) phase for which the lipid chain conformation is close to the S_o phase (33). It is known that the neuronal myelin contains 28% cholesterol and 23% cerebroside in weight (16), the two major lipid components of rafts that reside in the L_o phase (34). Using the polarization sensitivity of CARS (Fig. 4), the ordering degree of myelin lipids is characterized by the $I_{\parallel}/I_{\perp}$ ratio of 3.53. To relate this value with myelin composition, we studied the lipid ordering degree of myelin figures prepared by hydrating a lipid film of controlled composition (35). Based on the CARS images of typical myelin figures composed of DOPC, DPPC/cholesterol (40% in weight), or pure DPPC bilayers, the $I_{\parallel}/I_{\perp}$ values are measured to be 1.48, 4.44, and 6.21, respectively. For the myelin figures composed of DOPC, DPPC/cholesterol (40%), or pure DPPC, the bilayers

are in L_d, L_o, and S_o phases, respectively, at room temperature (36). Our results show that the lipid ordering degree of neuronal myelin ($I_\parallel/I_\perp = 3.53$) is closest to that of the DPPC/cholesterol myelin figure ($I_\parallel/I_\perp = 4.44$) which is in the L_o phase. Thus, we anticipate that myelin membranes are principally in the L_o phase (or rafts). As an additional evidence, the CARS spectral profile of a single myelin (Fig. 3) resembles that of S_o phase DSPC liposomes but differs from that of L_d phase DOPC liposomes (21) in the 2800–2900 cm^{-1} region. This also supports that the myelin lipids are in the L_o phase whose chain conformation is close to the S_o phase (37). Our result is consistent with the presence of detergent-insoluble glycolipid-enriched complexes in myelin membranes (38,39).

We have visualized that water molecules inside the myelin sheath are partially ordered (Fig. 5), providing direct evidence for the existence of structured water in biological systems. The ordered water produces a hydration force that prevents fusion of lipid bilayers (40). Despite extensive theoretical studies (41), it is difficult to selectively probe the membrane hydration water that is usually connected with the bulk water. The thick myelin sheath and the 3D sectioning capability of CARS microscopy permit us to probe the hydration water residing between adjacent bilayers. The ordered water was also observed in lipid onion structures by CARS microscopy (24).

Properties of CARS microscopy for tissue imaging

Unlike thin samples such as cell culture or polymer films in previous CARS microscopy studies (13,23), a tissue sample may significantly change the properties of optical beams due to its complexity (42). Here we discuss three key issues based on our CARS imaging results.

Spatial resolution

From CARS images of axonal myelin, the lateral and axial resolution of CARS microscopy have been determined to be 0.28 and 0.70 μm. These values are comparable to the values (0.28 and 0.75 μm) measured with 0.2 μm polystyrene bead embedded in an agarose gel (23).

Depth of detection

A large detection depth is critical for visualizing biological activities inside a thick tissue. TPEF microscopy provides larger depth than confocal fluorescence microscopy because it uses near infrared excitation wavelength. One major difference of CARS from TPEF lies in that it uses two collinearly overlapped beams. Optical aberration of the objective lens may scramble the overlap of the two beams focused into a tissue, which limits the depth of CARS imaging. Using the Olympus 60× water objective with a working distance of 280 μm, we are able to obtain nice F-CARS and E-CARS images of parallel axons 250-μm deep into the spinal cord sample. We should be able to increase the penetration depth by using an objective lens with a longer working distance. In addition, the penetration depth can be increased by using longer excitation wavelengths because the CARS signal does not need electronic resonance.

Polarization property

We have characterized the polarization property of CARS signals by using a large-area polarizer above the condenser. The F-CARS anisotropy for a coverslip glass under pure water, glass under a spinal cord sample, and myelin in our spinal cord sample is measured to be 0.99, 0.03, and 0.03, respectively, with $\omega_p - \omega_s$ tuned to 2840 cm^{-1}. This result indicates that the nonresonant CARS from glass is linearly polarized, but the polarization is totally scrambled after it passes through the tissue. The same process happens to F-CARS from the myelin. The major reason could be the myelin birefringence (43). On the other hand, the excitation polarization is well preserved when the laser beams are focused at the bottom of the samples. This allows us to analyze molecular orientation in a tissue sample based on the polarization selectivity of CARS (Figs. 4 and 5).

Combination of CARS and TPEF microscopy

TPEF and CARS microscopy have different advantages for neuron imaging. TPEF microscopy permits selective imaging of proteins and ions in neuron tissues (44) with the aid of highly specific probes (45,46), while CARS microscopy permits vibrational imaging of membranes without fluorophore labeling. As we have shown in Fig. 8, combining CARS and TPEF microscopy allows simultaneous imaging of axonal myelin and Ca^{2+}.

Both femto- and picosecond pulses have been used for TPEF imaging (2,47,48) and CARS imaging (9,49). To find out the suitable pulse width for combined CARS and TPEF imaging, we calculated the dependence of TPEF and CARS on the excitation pulse width. The theoretical models for computing the TPEF and CARS signals can be found elsewhere (2,49). The CARS signal is contributed by the third-order susceptibility that contains a vibrationally resonant and a nonresonant part. As shown in Fig. 9 *A*, the resonant CARS signal is saturated in the femtosecond region where the excitation spectral width is larger than the Raman line width (typically 10–20 cm^{-1}). The TPEF signal intensity is inversely proportional to the pulse duration (Fig. 9 *A*). In the picosecond region (>1 ps), the CARS signal drops faster than the TPEF signal because CARS has a higher nonlinearity. Fig. 9 *B* shows that the percentage of the resonant signal in the total CARS signal increases dramatically when the pulse duration increases from 100 fs to 1 ps. Then it gradually reaches a plateau after the pulse duration exceeds 2 ps. To produce a high-quality CARS

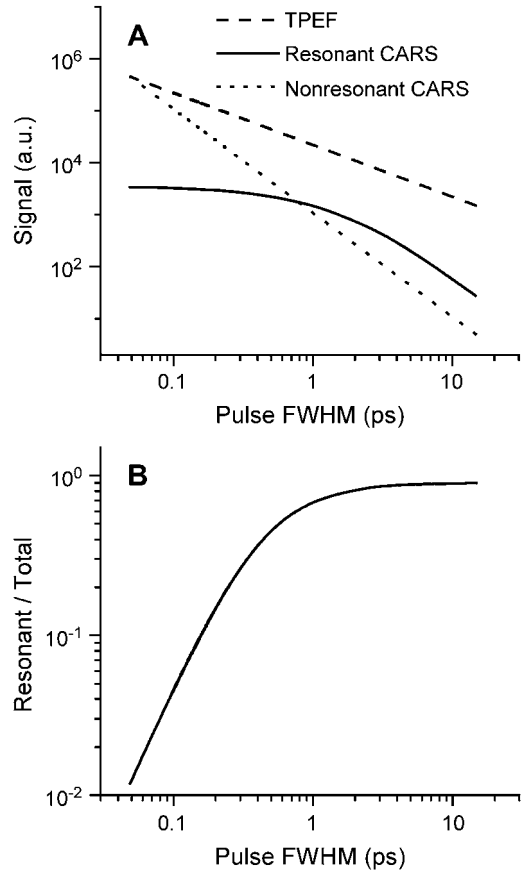

FIGURE 9 (*A*) Calculated CARS and TPEF signals as a function of the pulse duration. The resonant CARS signal is calculated from $\chi^{(3)R} = A/[\Omega - (\omega_p - \omega_s) - i\Gamma]$, where A, Ω, and Γ are the transition strength, the vibration frequency, and the Raman line half-width, respectively. Γ is set as 5 cm^{-1} and $\omega_p - \omega_s$ is tuned to Ω in the calculation. The nonresonant CARS signal is calculated from $\chi^{(3)NR}$, which is set to be $A/3\Gamma$ based on the signal/background ratio (10:1) of the CARS band for the CH_2 stretch vibration (Fig. 3). The TPEF signal is calculated with a model in the literature (2). (*B*) The ratio of the resonant CARS signal to the total CARS signal as a function of the pulse duration. The resonant CARS signal is calculated from $\chi^{(3)R}$; the total CARS signal is calculated from $\chi^{(3)} = \chi^{(3)NR} + \chi^{(3)R}$. We assume constant pulse energy and equal pulse widths between the pump and the Stokes beam in the calculation.

image, one needs a large resonant signal and a high ratio of the resonant signal to the nonresonant background. Therefore, a pulse width around 2.0 ps confers good CARS image quality as well as sufficient TPEF intensity.

Potentials of CARS microscopy for the study of spinal cord injury

Traumatic damage of spinal cord induces the loss of myelin sheath (50,51). Although EM studies have provided rich information about myelin morphology under different clinical conditions (15,52), it is hard to distinguish whether the observed change is from the injury or from the sample fixation and staining procedure. Additionally, the use of fixed tissues makes it impossible to follow the dynamics of myelin damage. The strong CARS signal from the symmetric CH_2 stretch vibration permits real-time imaging of changes in individual myelin following traumatic, anoxic, or ischemic insults. Moreover, it would be exciting to combine CARS with laser axotomy, in which a high-energy pulse induces ablation of single axons (53,54). Then CARS microscopy can be used to visualize neuronal regeneration.

Intracellular Ca^{2+} accumulation is a key indicator of anoxic, ischemic, or traumatic damage of neurons (55–58). Ca^{2+} dynamics in live cells and nerve fibers have been widely studied by confocal fluorescence and TPEF microscopy with the development of various Ca^{2+} indicators (31,59,60). With 2.5-ps pulses, we have demonstrated simultaneous CARS imaging of myelin and TPEF imaging of Ca^{2+} with Oregon green 488 (Fig. 8). The 3D spatial resolution of CARS and TEPF microscopy confers the capability of mapping Ca^{2+} distribution inside and outside the axon simultaneously, permitting real-time monitoring of Ca^{2+} influx into the axons. The reverse operation of the Na^+–Ca^{2+} exchanger is considered to be a primary route of Ca^{2+} entry during axon injury (61). However, direct observation is still lacking. Combining CARS with TPEF microscopy, we will be able to monitor the Ca^{2+} entry through the nodal axolemma that is enriched in Na^+ channels. Such an experiment will clarify the scenario of calcium-induced secondary damage.

Potentials of CARS microscopy for the study of demyelinating diseases

Diseases affecting the myelin sheath encompass a wide variety of both clinical and experimental conditions (62). The pathogenesis of multiple sclerosis and other demyelinating diseases still eludes researchers. The lateral resolution of CARS microscopy is sufficient for measuring the myelin sheath thickness and the *g* ratio (Fig. 6). Both are important parameters for judging demyelination. CARS microscopy provides a new approach to detecting disorders of myelin. For example, it can be applied to monitor chemically induced demyelination and possible remyelination processes in spinal tissues. Such a study will tell the timescale of demyelination, which cannot be accurately determined by electron microscopy studies of fixed tissues (63).

In addition, the CARS spectral profile provides information about molecular conformation such as the thermodynamic states of bilayers (21,64) and the secondary structure of proteins (65). Using a broadband pulse for the Stokes beam, multiplex CARS microscopy has been implemented on a scanning microscope (21,64,66). The capability of structural characterization can potentially be used to detect the pathology of the axonal myelin sheath (51,62).

CONCLUSIONS

We have shown that laser-scanning CARS microscopy permits 3D imaging of neuronal myelin under physiological

conditions. We have characterized the molecular orientation and vibrational spectral profile of myelin sheath in live spinal tissues. Our results show that myelin lipids are in the liquid ordered phase, with ordered water residing between adjacent bilayers. We have determined the *g* ratio of live axons. We have also observed the structure of the node of Ranvier and the Schmidt-Lanterman incisure under physiological conditions. Moreover, we have combined CARS with TPEF imaging for probing the intra- and extraaxonal calcium simultaneously. Our work demonstrates the potential of CARS microscopy for real-time imaging of neuronal myelin under different clinical conditions. CARS microscopy will be an important tool for the study of demyelinating diseases and spinal cord injury.

The authors acknowledge Jennifer M. McBride, and Ashley Nehrt for preparing the spinal tissue samples, and thank Jonathan Sutcliffe, Shannon Mesenbourg, Kathryn A. Antle, and Alan P. Kennedy for their help in the experiments.

This work was supported by a start-up fund from Purdue University, a Charles E. Culpepper Biomedical Pilot grant, and a fund from the state of Indiana.

REFERENCES

1. Helmchen, F., and W. Denk. 2002. New developments in multiphoton microscopy. *Curr. Opin. Neurobiol.* 12:593–601.
2. Denk, W., J. H. Strickler, and W. W. Webb. 1990. Two-photon laser scanning fluorescence microscopy. *Science.* 248:73–76.
3. Mizrahi, A., J. C. Crowley, E. Shtoyerman, and L. C. Katz. 2004. High-resolution in vivo imaging of hippocampal dendrites and spines. *J. Neurosci.* 14:3147–3151.
4. Levene, M. J., D. A. Dombeck, K. A. Kasischke, R. P. Molloy, and W. W. Webb. 2004. In vivo multiphoton microscopy of deep brain tissue. *J. Neurophysiol.* 91:1908–1912.
5. Hellwarth, R., and P. Christensen. 1974. Nonlinear optical microscopy examination of structure in polycrystalline ZnSe. *Opt. Commun.* 12: 318–322.
6. Moreaux, L., O. Sandre, and J. Mertz. 2000. Membrane imaging by second-harmonic generation microscopy. *J. Opt. Soc. Am. B.* 17:1685–1694.
7. Campagnola, P. J., and L. M. Loew. 2003. Second-harmonic imaging microscopy for visualizing biomolecular arrays in cells, tissues and organisms. *Nat. Biotechnol.* 21:1356–1360.
8. Duncan, M. D., J. Reintjes, and T. J. Manuccia. 1982. Scanning coherent anti-Stokes Raman microscope. *Opt. Lett.* 7:350–352.
9. Zumbusch, A., G. R. Holtom, and X. S. Xie. 1999. Three-dimensional vibrational imaging by coherent anti-Stokes Raman scattering. *Phys. Rev. Lett.* 82:4142–4145.
10. Cheng, J. X., and X. S. Xie. 2004. Coherent anti-Stokes Raman scattering microscopy: instrumentation, theory, and applications. *J. Phys. Chem. B.* 108:827–840.
11. Shen, Y. R. 1984. The Principles of Nonlinear Optics. John Wiley and Sons, New York, NY.
12. Potma, E. O., and X. S. Xie. 2003. Detection of single lipid bilayers in coherent anti-Stokes Raman scattering (CARS) microscopy. *J. Raman Spectrosc.* 34:642–650.
13. Potma, E. O., X. S. Xie, L. Muntean, J. Preusser, D. Jones, J. Ye, S. R. Leone, W. D. Hinsberg, and W. Schade. 2004. Chemical imaging of photoresists with coherent anti-Stokes Raman scattering (CARS) microscopy. *J. Phys. Chem.* 108:1296–1301.
14. Nan, X., J. X. Cheng, and X. S. Xie. 2003. Vibrational imaging of lipid droplets in live fibroblast cells using coherent anti-Stokes Raman microscopy. *J. Lipid Res.* 40:2202–2208.
15. Hirano, A., and J. F. Liena. 1995. Morphology of central nervous system axons. *In* The Axon Structure, Function and Pathophysiology. S. G. Waxman, J. D. Kocsis, and P. K. Stys, editors. Oxford University Press, New York, NY. 49–67.
16. Morell, P., R. H. Quarles, and W. T. Norton. 1994. Myelin formation, structure, and biochemistry. *In* Basic Neurochemistry: Molecular, Cellular, and Medical Aspects, 5th Ed. G. J. Siegel, B. W. Agranoff, R. W. Alberts, and P. B. Molinoff, editors. Raven Press, New York, NY.
17. Pézolet, M., and D. Georgescauld. 1985. Raman spectroscopy of nerve fibers: a study of membrane lipids under steady-state conditions. *Biophys. J.* 47:367–372.
18. Shi, R., and A. R. Blight. 1997. Differential effects of low and high concentrations of 4-aminopyridine on axonal conduction in normal and injured spinal cord. *Neuroscience.* 77:553–562.
19. Shi, R., and R. Borgens. 1999. Acute repair of crushed guinea pig spinal cord by polyethylene glycol. *J. Neurophysiol.* 81:2406–2414.
20. Carey, D. M., and G. M. Korenowski. 1998. Measurement of the Raman spectrum of liquid water. *J. Chem. Phys.* 108:2669–2675.
21. Cheng, J. X., A. Volkmer, L. D. Book, and X. S. Xie. 2002. Multiplex coherent anti-Stokes Raman scattering microspectroscopy and study of lipid vesicles. *J. Phys. Chem.* 106:8493–8498.
22. Cheng, J. X., A. Volkmer, and X. S. Xie. 2002. Theoretical and experimental characterization of coherent anti-Stokes Raman scattering microscopy. *J. Opt. Soc. Am. B.* 19:1363–1375.
23. Cheng, J. X., Y. K. Jia, G. Zheng, and X. S. Xie. 2002. Laser-scanning coherent anti-Stokes Raman scattering microscopy and applications to cell biology. *Biophys. J.* 83:502–509.
24. Cheng, J. X., S. Pautot, D. A. Weitz, and X. S. Xie. 2003. Ordering of water molecules between phospholipid bilayers visualized by coherent anti-Stokes Raman scattering microscopy. *Proc. Natl. Acad. Sci. USA.* 100:9826–9830.
25. Donaldson, H. H., and G. W. Hoke. 1905. On the areas of the axis cylinder and medullary sheath as seen in cross sections of the spinal nerves of vertebrates. *J. Comp. Neurol.* 15:1–16.
26. Guy, J., E. A. Ellis, K. Kelley, and G. M. Hope. 1989. Spectra of G ratio, myelin sheath thickness, and axon and fiber diameter in the guinea pig optic nerve. *J. Comp. Neurol.* 287:446–454.
27. Goldman, L., and J. S. Albus. 1968. Computation of impulse conduction in myelinated fibres: theoretical basis of the velocity-diameter relation. *Biophys. J.* 8:596–607.
28. Raine, C. S. 1998. Neurocellular anatomy. *In* Basic Neurochemistry: Molecular, Cellular, and Medical Aspects, 6th Ed. G. J. Siegel, B. W. Agranoff, R. E. Albers, S. K. Fisher, and M. D. Uhler, editors. Raven Press, New York, NY.
29. Molander, M., C. H. Berthold, H. Persson, K. Andersson, and P. Fredman. 1997. Monosialoganglioside (GM1) immunofluorescence in rat spinal roots studied with a monoclonal antibody. *J. Neurocytol.* 26: 101–111.
30. Poliak, S., and E. Peles. 2003. The local differentiation of myelinated axons at nodes of Ranvier. *Nat. Rev. Neurosci.* 4:968–980.
31. Ren, Y., A. Ridsdale, E. Coderre, and P. K. Stys. 2000. Calcium imaging in live rat optic nerve myelinated axons in vitro using confocal laser microscopy. *J. Neurosci. Methods.* 102:165–176.
32. Saland, L. C., and L. M. Napolitano. 1977. Stabilization of cholesterol in myelin with digitonin: observation with polarized light. *J. Histochem. Cytochem.* 25:280–286.
33. Ipsen, J. H., G. Karlstrom, O. G. Mouritsen, H. Wennerstrom, and M. J. Zuckermann. 1989. Phase equilibria in the phosphatidyl-choline-cholesterol system. *Biochim. Biophys. Acta.* 905:162–172.
34. Brown, D. A., and E. London. 1998. Structure and origin of ordered domains in biological membranes. *J. Membr. Biol.* 164:103–114.
35. Harbich, W., and W. Helfrich. 1984. The swelling of egg lecithin in water. *Chem. Phys. Lipids.* 36:39–63.

36. Vist, M. R., and J. H. Davis. 1990. Phase equilibrium of cholesterol/dipalmitoylphosphatidylcholine mixtures: ^{2}H nuclear magnetic resonance and differential scanning calorimetry. *Biochemistry*. 29:451–464.

37. Simons, K., and W. L. C. Vaz. 2004. Model systems, lipid rafts, and cell membranes. *Annu. Rev. Biophys. Biomol. Struct.* 33:269–295.

38. Simons, M., E. M. Krämer, C. Thiele, W. Stoffel, and J. Trotter. 2000. Assembly of myelin by association of proteolipid protein with cholesterol- and galactosylceramide-rich membrane domains. *J. Cell Biol.* 151:143–153.

39. Erne, B., S. Sansano, M. Frank, and N. Schaeren-Wiemers. 2002. Rafts in adult peripheral nerve myelin contain major structural myelin proteins and myelin and lymphocyte protein (MAL) and CD59 as specific markers. *J. Neurochem.* 82:550–562.

40. McIntosh, T. J., and S. A. Simon. 1994. Hydration and steric pressures between phospholipid bilayers. *Annu. Rev. Biophys. Biomol. Struct.* 23: 27–51.

41. Marrink, S. J., and M. Berkowitz. 1995. Water and membranes. *In* Permeability and Stability of Lipid Bilayers. E. A. Disalvo and S. A. Simon, editors. CRC Press, Boca Raton, FL.

42. Cheong, W. F., S. A. Prahl, and A. J. Welch. 1990. A review of the optical properties of biological tissues. *IEEE J. Quantum Elect.* 26: 2166–2185.

43. Vidal, B. D. C., M. L. S. Mello, A. C. Caseiro-Filho, and C. Godo. 1980. Anisotropic properties of the myelin sheath. *Acta Histochem.* 66:32–39.

44. Tsai, P. S., N. Nishimura, E. J. Yoder, E. M. Dolnick, G. A. White, and D. Kleinfeld. 2002. Principles, design and construction of a two photon scanning microscope for in vitro and in vivo brain imaging. *In* In Vivo Optical Imaging of Brain Function. R. Frostig, editor. CRC Press, Boca Raton, FL. 113–171.

45. Tsien, R. Y. 1998. The green fluorescent protein. *Annu. Rev. Biochem.* 67:509–544.

46. Haugland, R. P. 2002. Handbook of Fluorescent Probes and Research Products, 9th Ed. Molecular Probes, Eugene, OR.

47. Koester, H. J., D. Baur, R. Uhl, and S. W. Hell. 1999. Ca^{2+} fluorescence imaging with pico- and femtosecond two-photon excitation: signal and photodamage. *Biophys. J.* 77:2226–2236.

48. Bewersdorf, J., and S. W. Hell. 1998. Picosecond pulsed two-photon imaging with repetition rates of 200 and 400 MHz. *J. Microsc.* 191:28–38.

49. Cheng, J. X., A. Volkmer, L. D. Book, and X. S. Xie. 2001. An epi-detected coherent anti-Stokes Raman scattering (E-CARS) microscope with high spectral resolution and high sensitivity. *J. Phys. Chem. B.* 105:1277–1280.

50. Gledhill, R. F., B. M. Harrison, and W. I. McDonald. 1973. Demyelination and remyelination after acute spinal cord compression. *Exp. Neurol.* 38:472–487.

51. Blight, A. R. 1985. Delayed demyelination and macrophage invasion: a candidate for secondary cell damage in spinal cord injury. *Cent. Nerv. Syst. Trauma.* 2:299–315.

52. Rosenbluth, J. 1995. Pathology of demyelinated and dysmyelinated axons. *In* The Axon Structure, Function and Pathophysiology. S. G. Waxman, J. D. Kocsis, and P. K. Stys, editors. Oxford University Press, New York, NY.

53. Yanik, M. F., H. Cinar, H. N. Cinar, A. D. Chisholm, Y. Jin, and A. Ben-Yakar. 2004. Functional regeneration after laser axotomy. *Nature.* 432:822.

54. Shi, R., J. H. Lucas, A. Wolf, and G. W. Gross. 1989. Calcium antagonists fail to protect mammalian spinal neurons after physical injury. *J. Neurotrauma.* 6:261–276.

55. Stys, P. K. 1998. Anoxic and ischemic injury of myelinated axons in CNS white matter: from mechanistic concepts to therapeutics. *J. Cereb. Blood Flow Metab.* 18:2–25.

56. Young, W. 1992. Role of calcium in central nervous system injuries. *J. Neurotrauma.* 9:S9–S25.

57. Kriestián, T., and B. K. Siesjö. 1996. Calcium-related damage in ischemia. *Life Sci.* 59:357–367.

58. Borgens, R. B., and R. Shi. 2000. Immediate recovery from spinal cord injury through molecular repair of nerve membranes with polyethylene glycol. *FASEB. J.* 14:27–35.

59. Stricker, S. A., and M. Whitaker. 1999. Confocal laser scanning microscopy of calcium dynamics in living cells. *Microsc. Res. Tech.* 46:356–369.

60. Stosiek, C., O. Garaschuk, K. Holthoff, and A. Konnerth. 2003. In vivo two-photon calcium imaging of neuronal networks. *Proc. Natl. Acad. Sci. USA.* 100:7319–7324.

61. LoPachin, R. M., and E. J. Lehning. 1997. Mechanism of calcium entry during axon injury and degeneration. *Toxicol. Appl. Pharmacol.* 143: 233–244.

62. Ludwin, S. K. 1995. Pathology of the myelin sheath. *In* The Axon Structure, Function and Pathophysiology. S. G. Waxman, J. D. Kocsis, and P. K. Stys, editors. Oxford University Press, New York, NY.

63. Hall, S. M., and N. A. Gregson. 1971. The in vivo and ultrastructural effects of injection of lysophosphatidyl choline into myelinated peripheral nerve fibers of the adult mouse. *J. Cell Sci.* 9:769–789.

64. Müller, M., and J. M. Schins. 2002. Imaging the thermodynamics state of lipid membranes with multiplex CARS microscopy. *J. Phys. Chem. B.* 106:3715–3723.

65. Voroshilov, A., C. Otto, and J. Greve. 1996. Secondary structure of bovine albumin as studied by polarization-sensitive multiplex CARS spectroscopy. *Appl. Spectrosc.* 50:78–85.

66. Otto, C., A. Voroshilov, S. G. Kruglik, and J. Greve. 2001. Vibrational bands of luminescent zinc(II)-octaethyl-porphyrin using a polarization-sensitive 'microscopic' multiplex CARS technique. *J. Raman Spectrosc.* 32:495–501.